# Efficient Light Bending with Isotropic Metamaterial Huygens' Surfaces

Carl Pfeiffer,[†] Naresh K. Emani,[‡] Amr M. Shaltout,[‡] Alexandra Boltasseva,[‡] Vladimir M. Shalaev,*[,‡] and Anthony Grbic*[,†]

[†]Department of Electrical Engineering and Computer Science, University of Michigan, Ann Arbor, Michigan 48109-2122, United States

[‡]School of Electrical and Computer Engineering and Birck Nanotechnology Center, Purdue University, West Lafayette, Indiana 47907, United States

**S** Supporting Information

**ABSTRACT:** Metamaterial Huygens' surfaces manipulate electromagnetic wavefronts without reflection. A broadband Huygens' surface that efficiently refracts normally incident light at the telecommunication wavelength of 1.5 μm is reported. The electric and magnetic responses of the surface are independently controlled by cascading three patterned, metallic sheets with a subwavelength overall thickness of 430 nm. The peak efficiency of the device is significantly enhanced by reducing the polarization and reflection losses that are inherent to earlier single-layer designs.



**KEYWORDS:** Metamaterial, metasurface, Huygens, lens, plasmonics
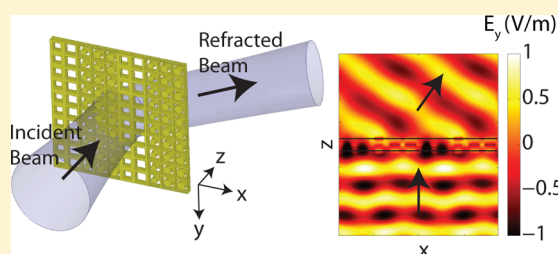
Metamaterials have received much attention due to their ability to provide extreme control of electromagnetic fields. However, at near-infrared and visible wavelengths, metamaterials have been hampered by fabrication challenges and high loss, significantly limiting their impact.[1] This has led to the development of metasurfaces: the two-dimensional equivalent of metamaterials.[2,3] Metasurfaces can impart discontinuities on electromagnetic wavefronts, giving them the ability to generate novel lenses for a myriad of nanophotonic applications including optical tweezing, image sensors, and displays.[4,5] In contrast, more conventional optics such as dielectric lenses and spatial light modulators are bulky, which limits their integration into nanophotonic systems.[6–9] Optical metasurfaces reported to date only manipulate electric polarization currents, which fundamentally limits their maximum efficiency due to polarization and reflection loss.[10–12] Efficiencies on the order of 5% are typical in these previous designs. In addition, many of these metasurfaces suffer from low phase coverage or only work for a single polarization.[4,13] This limits their ability to tailor an incident wavefront. In fact, the surface equivalence principle dictates that a magnetic response must be present for complete control of an electromagnetic wavefront by a surface.[14] This has led to the development of metamaterial Huygens' surfaces, which use collocated electric and magnetic polarizabilities to realize reflectionless low profile lenses.[15]

At microwave frequencies, generating a magnetic response is straightforward using split-ring-resonators.[16] However, this approach has its challenges at optical frequencies.[17] Alternatively, cascading metallic layers upon one another can also generate a magnetic response due to circulating electric currents.[18–20] This has led to the well-known fishnet structure, which provides both an electric and magnetic response to realize a negative index of refraction.[20] However, bulk metamaterials such as the fishnet structure generally exhibit relatively low phase shifts per unit cell as light propagates through them. In contrast, the inhomogeneous metasurfaces developed here exhibit large phase shifts across a subwavelength thickness. To date, optical metasurface designs that incorporate a magnetic response have been proposed, but no experiments have been performed.[21–23]

In this paper, the first experimental metamaterial Huygens' surface at optical frequencies is demonstrated. An isotropic unit cell consisting of cascaded sheet admittances (patterned metallic sheets) is proposed, and a straightforward design procedure is detailed. The magnetic response is generated by circulating, longitudinal electric currents supported by the cascaded metallic sheets. Simulations demonstrate that the proposed structure achieves large phase coverage while maintaining high transmission. A proof-of-concept metamaterial Huygens' surface is designed to refract normally incident light to an angle of 35° from normal at the design wavelength of 1.5 μm (see Figure 1). Simulations show that the surface exhibits a high efficiency of 30%, and an order of magnitude improvement in the extinction ratio over previously reported metasurfaces. The metamaterial Huygens' surface is then fabricated by sequentially patterning three gold (Au) sheets
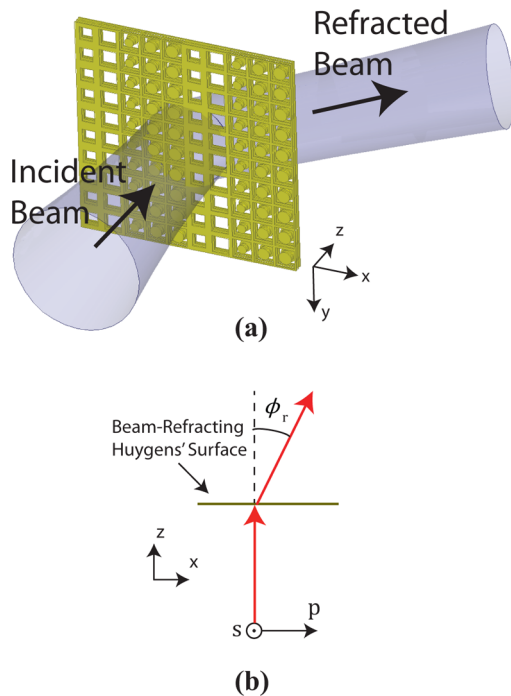
**Figure 1.** (a) Perspective view of an optically thin, isotropic metamaterial Huygens' surface that efficiently refracts a normally incident beam at telecommunication wavelengths. In contrast to previous designs, isotropic Huygens' surfaces are impedance matched to free space (exhibit low reflection) and can achieve complete phase coverage for the copolarized field with zero polarization loss. (b) Top view of the beam-refracting metamaterial Huygens' surface.

using standard electron beam lithography and liftoff processes, while employing SU-8 dielectric spacers between them. Measurements are performed using a spectroscopic ellipsometer, and the performance significantly exceeds previously reported metasurfaces. In addition, this work presents the first experimental demonstration of an isotropic metasurface that is capable of providing wavefront control for arbitrarily polarized light.

To begin, a unit cell is developed that exhibits high transmittance and large phase coverage. Consider a single, patterned metallic sheet. Provided its periodicity is subwavelength, any pattern can be represented as a well-defined, sheet admittance boundary condition with $Y_s \vec{E}_t = \vec{J}_s$, where $\vec{J}_s$ is the surface current on the metallic sheet, and $\vec{E}_t$ is the electric field tangential to the sheet. The sheet admittance ($Y_s$) is a scalar quantity since the patterns considered here are isotropic. The imaginary part of the sheet admittance can be controlled by changing the pattern on the metallic sheet. The real part of the sheet admittance represents metallic losses. Previous metasurfaces that only used a single sheet admittance to tailor light suffered from significant reflection loss, since electric currents are bidirectional radiators.[22] However, cascading multiple sheet admittances upon one another generates an additional magnetic response because the cascaded sheets can support longitudinal circulating electric currents.[24] With collocated electric and magnetic currents, each unit cell of the metasurface generates a unidirectional radiated field to realize a reflectionless Huygens' source.[25] Metasurfaces composed of reflectionless unit cells have come to be known as metamaterial Huygens' surfaces

since they manipulate electromagnetic wavefronts in the same manner Christiaan Huygens analyzed wavefront propagation.[26]

It has been shown that at least three sheet admittances (see Figure 2a) are required to obtain complete phase control while
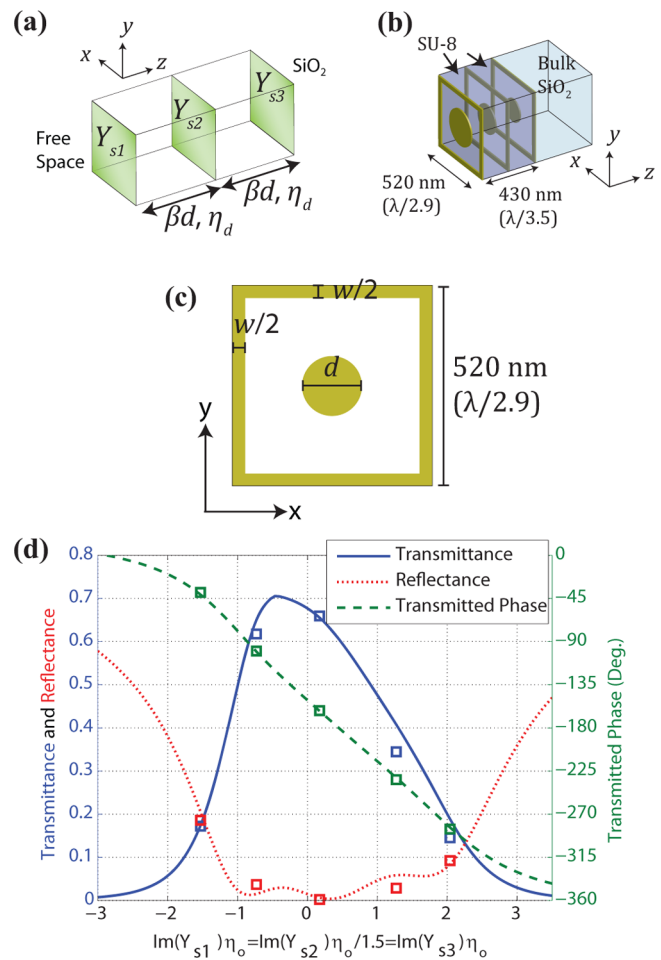


**Figure 2.** Unit cell design. (a) Analytic model of a unit cell comprising the metamaterial Huygens' surface. (b) Perspective view of a typical unit cell. (c) Top view of each of the three sheet admittances. The imaginary part of the sheet admittance increases with increasing "$d$", whereas the imaginary part of the sheet admittance decreases with increasing "$w$". It can be seen that the cell is isotropic. Therefore, there is no scattered power in the cross-polarized field component. (d) Transmittance, transmitted phase, and reflectance as a function of the imaginary part of the outer sheet admittances ($Y_{s1} = Y_{s3}$) at a wavelength of 1.5 $\mu$m. Light is incident from the SiO$_2$ substrate side. The squares indicate the simulated reflection and transmission coefficients of the five unit cells shown in Figure 3a. It is assumed the middle sheet admittance is 1.5 times the outer sheet admittances ($Y_{s1} = Y_{s3} = Y_{s2}/1.5$), which limits reflection loss. The loss of the sheet admittance is estimated from simulations of the unit cell shown in part (b) (see Supporting Information Figure S4).

maintaining high transmittance.[22,24] To realize the sheet admittances, the geometry shown in Figure 2b is chosen.[23] The unit cell is isotropic and consists of three 30 nm thick Au sheets patterned on a SiO$_2$ substrate. The Au sheets are separated by 200 nm thick SU-8 dielectric spacers to realize an overall thickness of 430 nm ($\lambda_o/3.5$). It should be emphasized that it is more appropriate to model this structure as a two-dimensional metasurface rather than a bulk metamaterial because it exhibits large phase shifts across a subwavelength

overall thickness.[27] However, this is somewhat of an approximation due to the notable thickness. The SiO$_2$ substrate is modeled as a lossless, infinite half space with an index of refraction of $n_{SiO_2}$ = 1.45. The index of refraction of the SU-8 is $n_{SU-8}$ = 1.57. The relative permittivity of Au is described by the Drude model $\varepsilon_{Au} = \varepsilon_\infty - \omega_p^2/(\omega^2 + j\omega\omega_c)$, with $\varepsilon_\infty$ = 9.0, plasma frequency $\omega_p$ = 1.363 × 10$^{16}$ rad/s (8.97 eV), and collision frequency $\omega_c$ = 3.60 × 10$^{14}$ rad/s (0.24 eV). This collision frequency assumes a loss that is over three times that of bulk Au,[28] which takes into account thin film surface scattering and grain boundary effects.[29] Each of the three sheet admittances can be modeled as a parallel LC circuit (see Figure 2c). The inductance arises from both electron inertia and the wire grid outlining each unit cell. The capacitance is created by the central disk. This structure is similar to the well-known fishnet structure with the primary difference being that the capacitive patches do not touch the wire grid.[20,30] This difference increases inductance and reduces capacitance, which in turn enhances the bandwidth near the resonance (see Supporting Information Figure S5). A useful feature of cascaded sheet admittances is that their reflection and transmission properties can be solved in closed form by employing the transfer matrix (ABCD) approach (see Supporting Information). In Figure 2d, the transmittance, transmitted phase, and reflectance are plotted as a function of the outer sheet admittances ($Y_{s1} = Y_{s3}$). From the analytic model that includes losses (see Supporting Information Figure S4), it was found that enforcing the condition $Y_{s1} = Y_{s3} = Y_{s2}/1.5$, provides a good trade-off between maximizing transmission bandwidth and phase coverage, while minimizing loss and reflection. It should be noted that transmittance and phase coverage increase with reduced metallic loss.
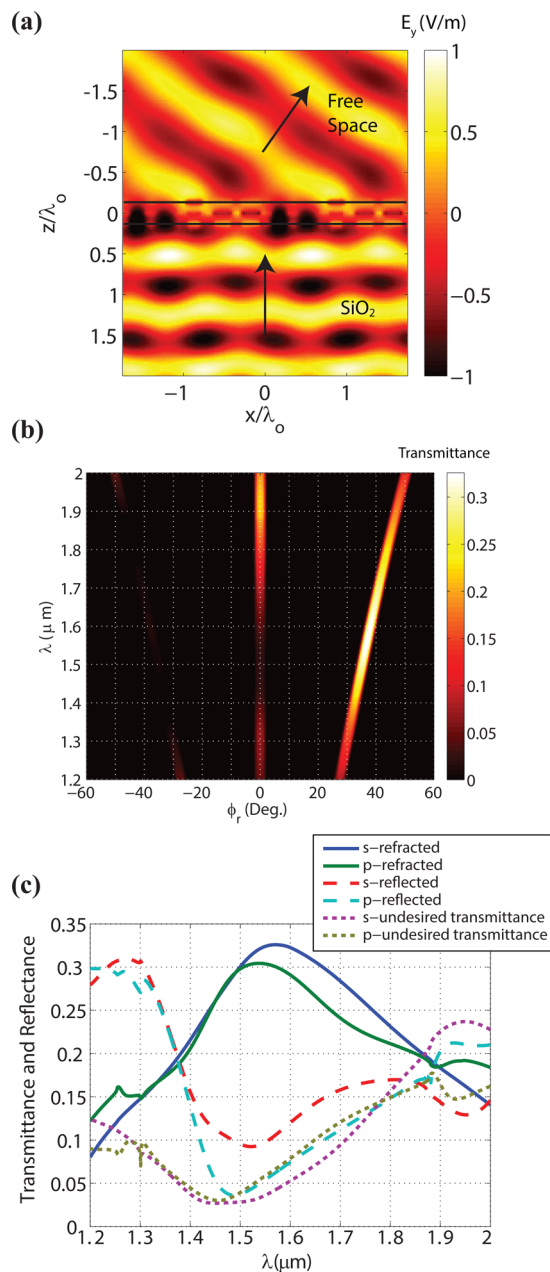
A beam-refracting metamaterial Huygens' surface is then realized by stipulating a linear phase progression across the surface.[11] This example was chosen because its performance is straightforward to characterize in experiment.[10] In future work, elaborate phase profiles can be stipulated to achieve more exotic wavefronts. Figure 3a shows a section of the designed Huygens' surface that refracts normally incident light to an angle of 35.2° at a wavelength of 1.5 μm. Further design details and exact dimensions are supplied in Table S1 of the Supporting Information. Each supercell contains five unit cells whose simulated performance is shown in Figure 2d. Simulations were performed using the full-wave solver, CST Microwave Studio. It can be seen that there is a good agreement between the simulated data points and the analytic model. Figure 3b,c shows the wavelength dependence of the transmittance and transmitted phase shift of the five unit cells. It should be noted that the achievable phase coverage was reduced due to Au loss. If the minimum transmittance of each unit cell is stipulated to be 0.15, the achievable phase coverage is limited to 260° rather than the ideal 360°. In addition, the transmittances of each unit cell are not identical. Both the reduced phase coverage and nonidentical transmittance creates aberration in the transmitted field. For periodic structures such as beam-refracting surfaces, these aberrations can be easily quantified using well-known Floquet theory.[31] In short, the transmitted field can be decomposed into propagating Floquet harmonics. For example, transmission into the $n = 0$ harmonic corresponds to light that is transmitted in the normal direction ($\phi_r = 0°$), whereas the $n = 1$ harmonic corresponds the refracted direction ($\phi_r = 35.2°$). The goal here is to maximize
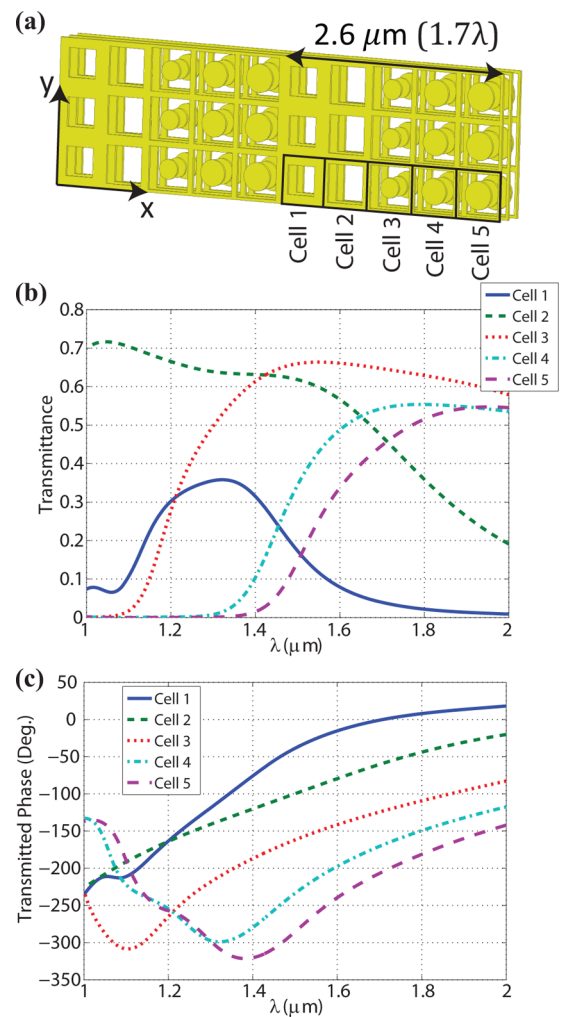


**Figure 3.** Designed beam-refracting Huygens' surface. (a) Perspective view of the metamaterial Huygens' surface when viewed from the bulk SiO$_2$ side. All dimensions are to scale. The five unit cells comprising the surface are outlined. (b,c) Simulated wavelength dependence of the transmittance and transmitted phase shift of each unit cell comprising the designed metamaterial Huygens' surface.

the power in the $n = 1$ harmonic, while minimizing the power in other harmonics.

The simulated performance of the designed metamaterial Huygens' surface is shown in Figure 4. Figure 4a shows a time snapshot of the steady-state electric field when a plane wave is normally incident from the SiO$_2$ substrate at a wavelength of 1.5 μm. It can be seen that the Huygens' surface efficiently refracts the incident light to $\phi_r = 35.2°$. The ripple in the field is from power that is scattered into undesired Floquet harmonics. In Figure 4b, the transmittance is plotted as a function of the refracted angle and wavelength. This shows the angular dependence of the various Floquet harmonics. It can be seen that the majority of the transmitted power is in the $n = 1$ harmonic. As the operating wavelength varies from 1.2 to 2 μm, the refracted angle of this harmonic scans from $\phi_r = 27.5°$ to $\phi_r = 50.3°$. The power that is refracted is better quantified in Figure 4c, which plots the transmittance and reflectance versus wavelength. In this plot, the s- and p-refracted curves correspond to the transmittance of the two polarizations into the $n = 1$ Floquet harmonic. Also shown are two of the loss mechanisms of the Huygens' surface, which include reflection

**(a)**



**(b)**



**(c)**



**Figure 4.** Simulated beam-refracting metamaterial Huygens' surface. (a) Time snapshot of the steady-state, $y$-polarized electric field when a plane wave is normally incident from the bottom at a wavelength of 1.5 $\mu$m. The incident electric field has an amplitude of 1 V/m. (b) Transmittance as a function of wavelength and transmitted angle for s-polarized light. At the design wavelength of 1.5 $\mu$m, the transmittance of the $n = 1$ Floquet harmonic ($\phi_r = 35.2°$) is much larger than the $n = -1$ ($\phi_r = -35.2°$) and $n = 0$ ($\phi_r = 0°$) harmonics. (c) Transmittance and reflectance versus wavelength for both polarizations. s- and p-refracted denotes the transmittance of light that is refracted into the $n = 1$ harmonic for the s- and p-polarizations, respectively. s- and p-reflected denotes the total reflectance. s- and p-undesired transmittance denotes the total transmittance that is not in the $n = 1$ harmonic. Virtually no power ($-60$ dB) is scattered into cross-polarized light.

and transmission into undesired Floquet harmonics (for example, $n = -2$, $n = -1$, $n = 0$, $n = 2$ harmonics). Virtually no power ($-60$ dB) is scattered into cross-polarized light. The power that is lost due to Au absorption is $1 -$ (refracted) $-$

(reflected) $-$ (transmitted undesired), which is approximately 60% at the wavelength of 1.5 $\mu$m. The metamaterial Huygens' surface is isotropic since the s- and p-polarized curves coincide over much of the operating wavelengths. The difference between the two polarizations is most likely due to the coupling between spatially varying unit cells since this is not accounted for in the analytic model. It should also be noted that the response is broadband. The refracted field maintains a transmittance that is greater than half its peak value over a bandwidth of 1.33 to 1.95 $\mu$m (38%) for both polarizations. Two important performance metrics are the peak efficiency (transmittance in the refracted direction) and extinction ratio (ratio of the refracted transmittance to normal transmittance).[12] Simulations demonstrate a peak efficiency and extinction ratio of 32.6% and 11.6 dB, respectively, for s-polarized light and 30.4% and 10.3 dB, respectively, for p-polarized light.
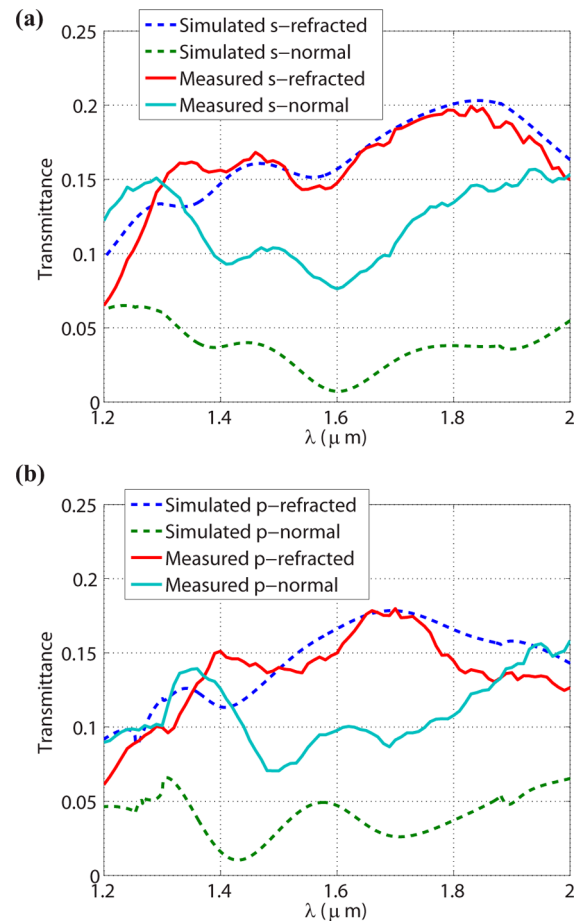
The fabrication process is shown in Figure 5a.[32] The design is fabricated on a 500 $\mu$m thick SiO$_2$ substrate. First, the bottom sheet admittance ($Y_{s3}$) is fabricated by patterning a 2 nm Ti adhesion layer and 28 nm Au layer using standard electron beam lithography and liftoff. Next, a 200 nm thick, SU-8 dielectric layer is spin coated onto the wafer, which naturally planarizes the surface for the following layer (measured roughness <5 nm). This process is repeated until three Au layers are patterned to achieve the unit cell shown in Figure 2b. The patterned area is 500 $\mu$m × 500 $\mu$m. Scanning electron microscope (SEM) pictures of the fabricated metamaterial Huygens' surface are shown in Figure 5 b,c.

The fabricated sample is measured using the transmission module of an ellipsometer (V-VASE, J. A. Woollam Co.) A monochromator scans the wavelength of a normally incident light source, and the transmitted power is measured at each refracted angle. Unlike in the simulations of Figure 4, the incident light in measurements propagates in the +z direction, which simplifies the alignment procedure. This has minimal effect on the transmittance but does increase the reflectance. Simulations suggest that when the incident light propagates in the +z direction, the refracted transmittance is at most 3% different from when the incident light propagates in the $-z$ direction. The measured transmittance in the refracted direction and normal direction are shown in Figure 6a,b for s-polarized and p-polarized light, respectively. From SEM pictures, the dimensions of the fabricated surface are off by ~30 nm, which causes the discrepancy between the measured performance and the simulations presented in Figure 4. To demonstrate that the difference between the fabricated and designed dimensions is the cause of error between measurement and simulation, the fabricated dimensions are also simulated, which is shown in Figure 6. It can be seen that the resimulated and measured performance agree for the refracted power. However, the power that is transmitted into the normal direction is still ~5% larger in measurement than simulation, but the trends are the same. The difference between simulation and measurement can be attributed to additional fabrication and measurement errors. If the fabricated sample is not centered on the incident beam for the ellipsometry measurements, a small percentage of the power is not captured by the metamaterial Huygens' surface. In addition, there is some uncertainty when modeling the surface roughness and loss of the Au, which introduces error into the simulations. Despite the various sources of error, these measurements achieve a peak efficiency and extinction ratio of 19.9% and 2.93
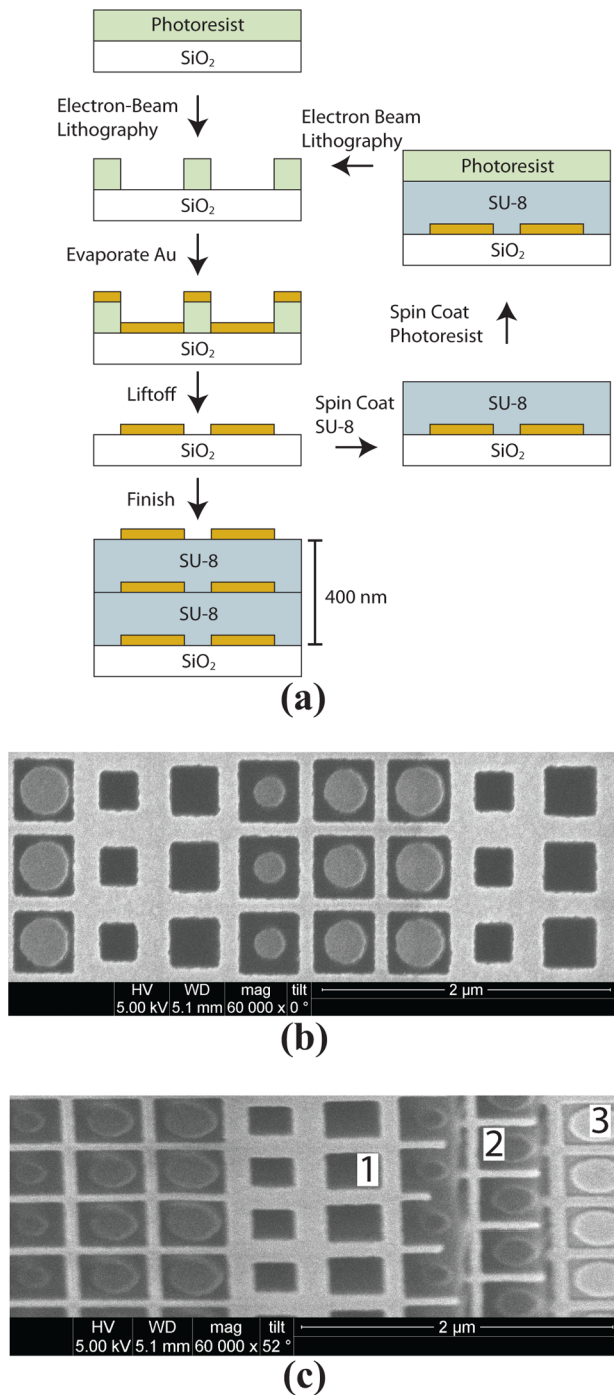
**Figure 5.** Fabrication of the metamaterial Huygens' surface. (a) Fabrication process involves sequential patterning of each 2 nm/28 nm thick Ti/Au layer using standard electron-beam lithography and liftoff, followed by spin coating of a 200 nm thick SU-8 dielectric layer. Three metallic layers are patterned using the process resulting in an overall thickness of 430 nm. (b) Scanning electron microscope (SEM) picture of a section of the metamaterial Huygens' surface. (c) Perspective view of the edge of the Huygens' surface, such that all three layers can be seen.



**Figure 6.** Transmittance measurement results. (a) Transmittance of s-polarized light into the refracted and normal directions versus wavelength. (b) Transmittance of p-polarized light into the refracted and normal directions versus wavelength. For both (a,b), the simulation values account for the fabricated dimensions of the Au patterns, which are off by ~30 nm from the design values based on SEM pictures.

dB, respectively, for s-polarized light and 18.0% and 3.05 dB, respectively, for p-polarized light. This is an improvement of a factor of 3 in efficiency and a factor of 4 in extinction ratio over the state of the art.[33] In addition, the response is isotropic, which enables control of an arbitrary incident polarization.

However, it should be noted that this increased performance does come at the expense of an increased thickness and a multilayer fabrication process.

A low profile metamaterial Huygens' surface is experimentally demonstrated for the first time at optical wavelengths. The efficiency is improved over previous metasurfaces by adding a magnetic response, which reduces reflection and polarization loss. In addition, the surface exhibits an isotropic response and large extinction ratio. In future work, the fabrication process can be further optimized so that the fabricated dimensions are closer to the design. In addition, large area soft lithography processes, such as nanoimprint lithography, can be used to dramatically reduce the cost of metasurfaces. This work can find numerous applications such as low profile lenses,[9] computer-generated-holography,[34] nondestructive evaluation,[35] and stealth technologies.[36] In addition, novel types of beams such as Airy beams,[37] Bessel beams,[38] and vortex beams[11] can be generated with high efficiency. By using anisotropic sheet admittances, polarization control such as linear-to-circular polarization conversion could also be achieved.[23,24,39]

## ■ AUTHOR INFORMATION

**Corresponding Authors**
*E-mail: shalaev@ecn.purdue.edu (V.M.S).
*E-mail: agrbic@umich.edu (A.G.).

**Notes**
The authors declare no competing financial interest.

## ■ REFERENCES

(1) Shalaev, V. M. Optical negative-index metamaterials. *Nat. Photonics* **2007**, *1* (1), 41–48.

(2) Holloway, C. L.; Kuester, E. F.; Gordon, J. A.; O'Hara, J.; Booth, J.; Smith, D. R. An overview of the theory and applications of metasurfaces: The two-dimensional equivalents of metamaterials. *IEEE Antennas Propag. Mag.* **2012**, *54* (2), 10–35.

(3) Kildishev, A. V.; Boltasseva, A.; Shalaev, V. M. Planar photonics with metasurfaces. *Science* **2013**, *339* (6125), 1232009.

(4) Verslegers, L.; Catrysse, P. B.; Yu, Z.; White, J. S.; Barnard, E. S.; Brongersma, M. L.; Fan, S. Planar lenses based on nanoscale slit arrays in a metallic film. *Nano Lett.* **2008**, *9* (1), 235–238.

(5) Grier, D. G. A revolution in optical manipulation. *Nature* **2003**, *424* (6950), 810–816.

(6) Lu, F.; Sedgwick, F. G.; Karagodsky, V.; Chase, C.; Chang-Hasnain, C. J. Planar high-numerical-aperture low-loss focusing reflectors and lenses using subwavelength high contrast gratings. *Opt. Express* **2010**, *18* (12), 12606–12614.

(7) Curtis, J. E.; Koss, B. A.; Grier, D. G. Dynamic holographic optical tweezers. *Opt. Commun.* **2002**, *207* (1), 169–175.

(8) Dufresne, E. R.; Spalding, G. C.; Dearing, M. T.; Sheets, S. A.; Grier, D. G. Computer-generated holographic optical tweezer arrays. *Rev. Sci. Instrum.* **2001**, *72* (3), 1810–1816.

(9) Aieta, F.; Genevet, P.; Kats, M. A.; Yu, N.; Blanchard, R.; Gaburro, Z.; Capasso, F. Aberration-free ultrathin flat lenses and axicons at telecom wavelengths based on plasmonic metasurfaces. *Nano Lett.* **2012**, *12* (9), 4932–4936.

(10) Ni, X.; Emani, N. K.; Kildishev, A. V.; Boltasseva, A.; Shalaev, V. M. Broadband light bending with plasmonic nanoantennas. *Science* **2012**, *335* (6067), 427.

(11) Yu, N.; Genevet, P.; Kats, M. A.; Aieta, F.; Tetienne, J.-P.; Capasso, F.; Gaburro, Z. Light propagation with phase discontinuities: generalized laws of reflection and refraction. *Science* **2011**, *334* (6054), 333–337.

(12) Ni, X.; Ishii, S.; Kildishev, A. V.; Shalaev, V. M. Ultra-thin, planar, Babinet-inverted plasmonic metalenses. *Light: Sci. Appl.* **2013**, *2* (4), e72.

(13) Lin, L.; Goh, X. M.; McGuinness, L. P.; Roberts, A. Plasmonic lenses formed by two-dimensional nanometric cross-shaped aperture arrays for Fresnel-region focusing. *Nano Lett.* **2010**, *10* (5), 1936–1940.

(14) Balanis, C. A. *Antenna theory: analysis and design*; John Wiley & Sons: New York, 2012.

(15) Pfeiffer, C.; Grbic, A. Metamaterial huygens' surfaces: Tailoring wave fronts with reflectionless sheets. *Phys. Rev. Lett.* **2013**, *110* (19), 197401.

(16) Smith, D. R.; Padilla, W. J.; Vier, D.; Nemat-Nasser, S. C.; Schultz, S. Composite medium with simultaneously negative permeability and permittivity. *Phys. Rev. Lett.* **2000**, *84* (18), 4184.

(17) Merlin, R. Metamaterials and the Landau–Lifshitz permeability argument: large permittivity begets high-frequency magnetism. *Proc. Natl. Acad. Sci. U.S.A.* **2009**, *106* (6), 1693–1698.

(18) Lomakin, V.; Fainman, Y.; Urzhumov, Y.; Shvets, G. Doubly negative metamaterials in the near infrared and visible regimes based on thin film nanocomposites. *Opt. Express* **2006**, *14* (23), 11164–11177.

(19) Shalaev, V. M.; Cai, W.; Chettiar, U. K.; Yuan, H.-K.; Sarychev, A. K.; Drachev, V. P.; Kildishev, A. V. Negative index of refraction in optical metamaterials. *Opt. Lett.* **2005**, *30* (24), 3356–3358.

(20) Valentine, J.; Zhang, S.; Zentgraf, T.; Ulin-Avila, E.; Genov, D. A.; Bartal, G.; Zhang, X. Three-dimensional optical metamaterial with a negative refractive index. *Nature* **2008**, *455* (7211), 376–379.

(21) Memarzadeh, B.; Mosallaei, H. Array of planar plasmonic scatterers functioning as light concentrator. *Opt. Lett.* **2011**, *36* (13), 2569–2571.

(22) Monticone, F.; Estakhri, N. M.; Alù, A. Full control of nanoscale optical transmission with a composite metascreen. *Phys. Rev. Lett.* **2013**, *110* (20), 203903.

(23) Pfeiffer, C.; Grbic, A. Cascaded metasurfaces for complete phase and polarization control. *Appl. Phys. Lett.* **2013**, *102*, 231116.

(24) Pfeiffer, C.; Grbic, A. Millimeter-Wave Transmitarrays for Wavefront and Polarization Control. *IEEE Trans. Microwave Theory Tech* **2013**, *61* (12), 4407–4417.

(25) Jin, P.; Ziolkowski, R. W. Metamaterial-inspired, electrically small Huygens sources. *IEEE Antennas Wireless Propag. Lett.* **2010**, *9*, 501–505.

(26) Huygens, C. *Traité de la Lumière*; Pieter van der Aa: Leyden, 1690.

(27) Holloway, C. L.; Dienstfrey, A.; Kuester, E. F.; O'Hara, J. F.; Azad, A. K.; Taylor, A. J. A discussion on the interpretation and characterization of metafilms/metasurfaces: The two-dimensional equivalent of metamaterials. *Metamaterials* **2009**, *3* (2), 100–112.

(28) Johnson, P. B.; Christy, R.-W. Optical constants of the noble metals. *Phys. Rev. B* **1972**, *6* (12), 4370.

(29) Chen, K.-P.; Drachev, V. P.; Borneman, J. D.; Kildishev, A. V.; Shalaev, V. M. Drude relaxation rate in grained gold nanoantennas. *Nano Lett.* **2010**, *10* (3), 916–922.

(30) Zhang, S.; Fan, W.; Malloy, K.; Brueck, S.; Panoiu, N.; Osgood, R. Near-infrared double negative metamaterials. *Opt. Express* **2005**, *13* (13), 4922–4930.

(31) Larouche, S.; Smith, D. R. Reconciliation of generalized refraction with diffraction theory. *Opt. Lett.* **2012**, *37* (12), 2391–2393, DOI: 10.1364/OL.37.002391.

(32) Liu, N.; Guo, H.; Fu, L.; Kaiser, S.; Schweizer, H.; Giessen, H. Three-dimensional photonic metamaterials at optical frequencies. *Nat. Mater.* **2007**, *7* (1), 31–37.

(33) Liu, J.; Shaltout, A. M.; Ni, X.; Shalaev, V. M.; Kildishev, A. V. Experimental validation of a new bianisotropic parameter retrieval technique using plasmonic metasurfaces made of V-shape antennas. *Proc. SPIE* **2013**, *8806*, 88060F–88060F-10.

(34) Larouche, S.; Tsai, Y.-J.; Tyler, T.; Jokerst, N. M.; Smith, D. R. Infrared metamaterial phase holograms. *Nat. Mater.* **2012**, *11* (5), 450–454.

(35) Planchon, T. A.; Gao, L.; Milkie, D. E.; Davidson, M. W.; Galbraith, J. A.; Galbraith, C. G.; Betzig, E. Rapid three-dimensional isotropic imaging of living cells using Bessel beam plane illumination. *Nat. Methods* **2011**, *8* (5), 417–423.

(36) Avitzour, Y.; Urzhumov, Y. A.; Shvets, G. Wide-angle infrared absorber based on a negative-index plasmonic metamaterial. *Phys. Rev. B* **2009**, *79* (4), 045131.

(37) Zhang, P.; Hu, Y.; Li, T.; Cannan, D.; Yin, X.; Morandotti, R.; Chen, Z.; Zhang, X. Nonparaxial Mathieu and Weber accelerating beams. *Phys. Rev. Lett.* **2012**, *109* (19), 193901.

(38) Durnin, J.; Miceli, J. J.; Eberly, J. Diffraction-free beams. *Phys. Rev. Lett.* **1987**, *58* (15), 1499−1501.

(39) Yu, N.; Aieta, F.; Genevet, P.; Kats, M. A.; Gaburro, Z.; Capasso, F. A broadband, background-free quarter-wave plate based on plasmonic metasurfaces. *Nano Lett.* **2012**, *12* (12), 6328−6333.

Supporting Information for:

# Efficient Light Bending with Isotropic Metamaterial Huygens' Surfaces

*Carl Pfeiffer[†], Naresh K. Emani[‡], Amr M. Shaltout[‡], Alexandra Boltasseva[‡], Vladimir M. Shalaev*[‡], and Anthony Grbic*[†]*

[†]Department of Electrical Engineering and Computer Science, University of Michigan, Ann Arbor, Michigan 48109-2122, USA

[‡] School of Electrical & Computer Engineering and Birck Nanotechnology Center, Purdue University, West Lafayette, Indiana 47907, USA

**Corresponding Authors**

*E-mail: shalaev@ecn.purdue.edu (V.M.S); agrbic@umich.edu (A.G.)

# Supporting Information

**Reflection and transmission coefficients of cascaded sheet admittances**

The reflection and transmission coefficients of the geometry shown in Figure 2(a) of the main text can be solved in closed form using the transfer matrix ($ABCD$) approach.[1] This approach is valid so long as the sheets are sufficiently far from each other such that evanescent coupling between them can be neglected.
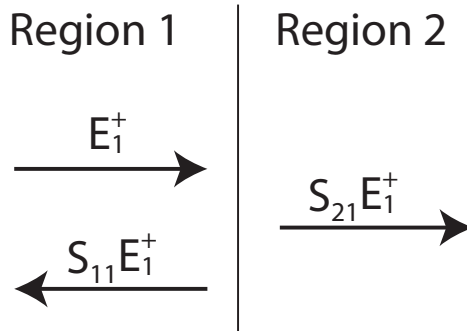
The $ABCD$ matrix of an arbitrary structure is defined as,

$$\begin{pmatrix} E_1 \\ H_1 \end{pmatrix} = \begin{pmatrix} A & B \\ C & D \end{pmatrix} \begin{pmatrix} E_2 \\ H_2 \end{pmatrix}, \tag{s1}$$

where $E_{1,2}$ and $H_{1,2}$ represent the total electric and magnetic fields on either side of the structure as shown in Figure S1. The S-parameters of an arbitrary structure are defined as,

$$\begin{pmatrix} E_1^- \\ E_2^- \end{pmatrix} = \begin{pmatrix} S_{11} & S_{21} \\ S_{12} & S_{22} \end{pmatrix} \begin{pmatrix} E_1^+ \\ E_2^+ \end{pmatrix}, \tag{s2}$$

where $E_{1,2}^+$ represents the electric field of a plane wave incident from Regions 1 and 2, respectively. $E_{1,2}^-$ represents the electric field of the plane wave reflected/transmitted into Regions 1 and 2, respectively. For example, $S_{11}$ is the reflection coefficient looking from Region 1 and $S_{21}$ is the transmission coefficient from Region 1 to Region 2.



**Figure S1**: Two regions of space separated by an arbitrary structure with reflection coefficient equal to $S_{11}$ and transmission coefficient equal to $S_{21}$.

By enforcing the boundary condition $Y_s \vec{E_t} = \vec{J_s}$, it can be shown that the $ABCD$ matrix of an isotropic sheet admittance of value $Y_s$ is equal to,[1]

$$\begin{pmatrix} A & B \\ C & D \end{pmatrix} = \begin{pmatrix} 1 & 0 \\ Y_s & 1 \end{pmatrix}. \tag{s3}$$

The $ABCD$ matrix of the dielectric separating each sheet admittance can be written as,[1]

$$\begin{pmatrix} \cos(\beta d) & j\eta_d \sin(\beta d) \\ j\sin(\beta d)/\eta_d & \cos(\beta d) \end{pmatrix}. \tag{s4}$$

Therefore, the $ABCD$ matrix of the cascaded sheet admittances shown in Figure S2 can be written as a product of the matrices of the individual components,

$$\begin{pmatrix} A & B \\ C & D \end{pmatrix} = \begin{pmatrix} 1 & 0 \\ Y_{s1} & 1 \end{pmatrix} \begin{pmatrix} \cos(\beta d) & j\eta_d \sin(\beta d) \\ \dfrac{j\sin(\beta d)}{\eta_d} & \cos(\beta d) \end{pmatrix} \begin{pmatrix} 1 & 0 \\ Y_{s2} & 1 \end{pmatrix}$$
$$\cdot \begin{pmatrix} \cos(\beta d) & j\eta_d \sin(\beta d) \\ \dfrac{j\sin(\beta d)}{\eta_d} & \cos(\beta d) \end{pmatrix} \begin{pmatrix} 1 & 0 \\ Y_{s3} & 1 \end{pmatrix}. \tag{s5}$$

Once the $ABCD$ matrix of the reciprocal structure is found, its S-parameters can be solved for using the following relation,

$$\begin{pmatrix} S_{11} & S_{12} \\ S_{21} & S_{22} \end{pmatrix} \tag{s6}$$
$$= \begin{pmatrix} \dfrac{A + B/\eta_2 - C\eta_1 - D\,\eta_1/\eta_2}{A + B/\eta_2 + C\eta_1 + D\,\eta_1/\eta_2} & \dfrac{2}{A\,\eta_2/\eta_1 + B/\eta_1 + C\eta_2 + D} \\ \dfrac{2}{A + B/\eta_2 + C\eta_1 + D\,\eta_1/\eta_2} & \dfrac{-A + B/\eta_2 - C\eta_1 + D\,\eta_1/\eta_2}{A + B/\eta_2 + C\eta_1 + D\,\eta_1/\eta_2} \end{pmatrix}.$$

It is assumed the wave impedance in Regions 1 and 2 are $\eta_1 = \sqrt{\mu_1/\varepsilon_1}$ and $\eta_2 = \sqrt{\mu_2/\varepsilon_2}$, respectively. It should be noted that the transmittance from Region 1 to Region 2 is equal to $|S_{21}|^2\sqrt{\eta_1/\eta_2}$. By inserting (s5) into (s6), the reflection and transmission coefficients of the cascaded sheet admittance are solved for in terms of the dielectric and cascaded sheet admittances.
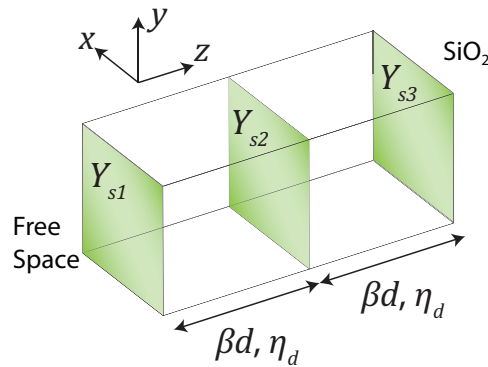


**Figure S2**: Cascaded sheet admittance model of a unit cell comprising the Huygens' surface.

**Sheet admittance realization**

   Once the desired sheet admittance is determined, its physical realization is designed through scattering simulations using CST Microwave Studio. As mentioned in the main text, the geometry shown in Figure S3(a) is employed to achieve arbitrary sheet admittances. Figure S3(b) demonstrates how the sheet is simulated. Floquet ports are used to excite normally incident plane waves. The ports are de-embedded to the $z = 0$ plane. Infinite periodicity is assumed by using periodic boundary conditions along the other four sides. However, this is an approximation since unit cells with different geometries will eventually be placed next to each other to generate a linear phase progression. The assumption of infinite periodicity is valid so long as the phase progression is not too steep, which is known as the local periodicity approximation.[2-5] As shown in Figure S3(b), the sheet admittance is in general located between two different media with wave impedances given by $\eta_1$ and $\eta_2$. For example, $Y_{s1}$ in the main text is located between SU-8 and free space. It is important to note that, in addition to the metallic pattern, the sheet admittance is also a function of the media surrounding it.
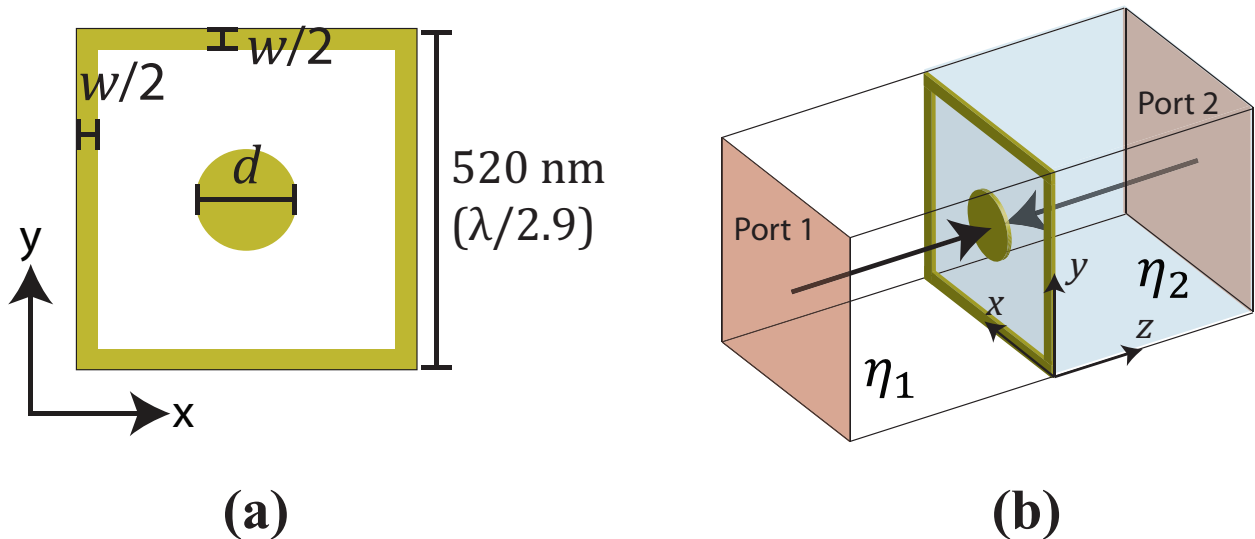


**Figure S3: (a)** Top view of each sheet admittance. **(b)** Simulation used to design the sheet admittance.

   An iterative approach is used to design the sheet admittance. First, initial dimensions 'w' and 'd' are stipulated and the structure is simulated. The single sheet admittance ($Y_s$) can be extracted from the simulated reflection coefficients,

$$Y_s = \frac{(S_{11} - 1)\eta_2 + (S_{11} + 1)\eta_1}{-(1 + S_{11})\eta_1\eta_2} = \frac{(S_{22} - 1)\eta_1 + (S_{22} + 1)\eta_2}{-(1 + S_{22})\eta_1\eta_2}. \tag{s7}$$

Then assuming that the sheet admittance can be modeled as a parallel LC circuit, the dimensions are adjusted while also attempting to maximize bandwidth and minimize loss. Near resonance, increasing 'w' decreases the imaginary part of the sheet admittance, whereas increasing 'd' increases the imaginary part of the sheet admittance. Once the sheet admittances are realized, their cascaded response can be calculated using the transfer matrix approach described earlier.

The imaginary part of the sheet admittance is primarily responsible for controlling the phase delay through a unit cell, and the real part accounts for the loss. For an accurate model of the cascaded sheet admittances, the relationship between the real and imaginary parts of the sheet admittance must be determined. From simulations of the geometry shown in Figure S3, it was found that the real part of the sheet admittance increases nearly monotonically with the magnitude of the imaginary part of the sheet admittance, as shown in Figure S4. This relationship between the real and imaginary parts of the sheet admittance is incorporated in the analytic model presented in Figure 2 of the main text.
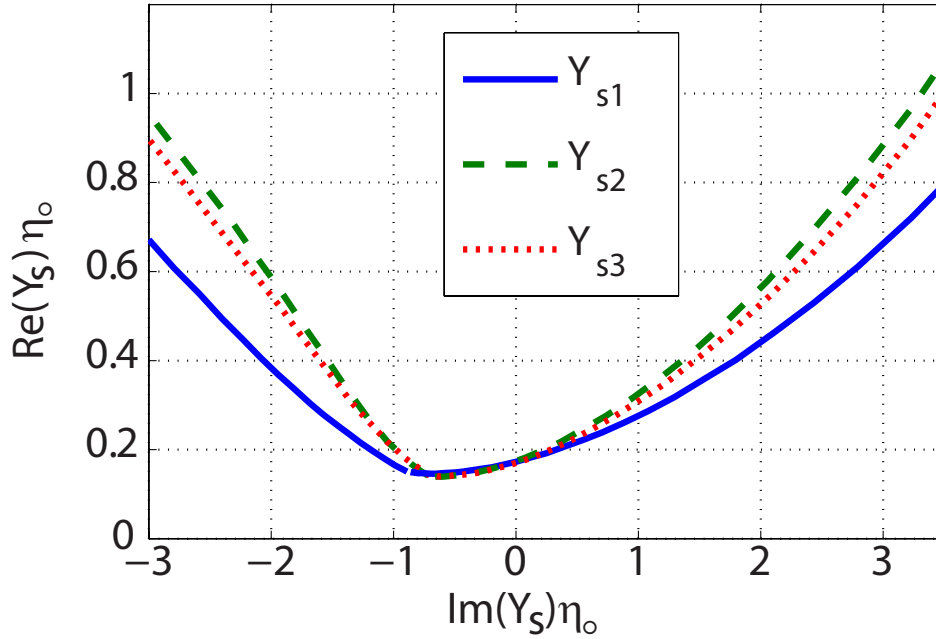


**Figure S4:** Relationship between the real and imaginary parts of each sheet admittance.

## Comparison to fishnet structure

It was mentioned that the proposed geometry shown in the main text (see Figure 2(c)) exhibits a larger bandwidth than the well-known fishnet structure.[6] To illustrate this, consider the unit cells shown in Figure S5(a) and S5(b). For the polarization shown, Figure S5(a) has an identical operation as the geometry presented in the main text (see Figure 2(c)), whereas Figure S5(b) is the fishnet geometry. Both structures are similar since they can be modeled as parallel LC circuits. The dimension 'w' primarily affects the inductance and 'd' primarily affects the capacitance. Both geometries can also be made to resonate at the same frequency. However, the geometry shown in Figure S5(a) has a larger inductance and correspondingly smaller capacitance than the geometry shown in Figure S5(b).

**(a)**                                                    **(b)**
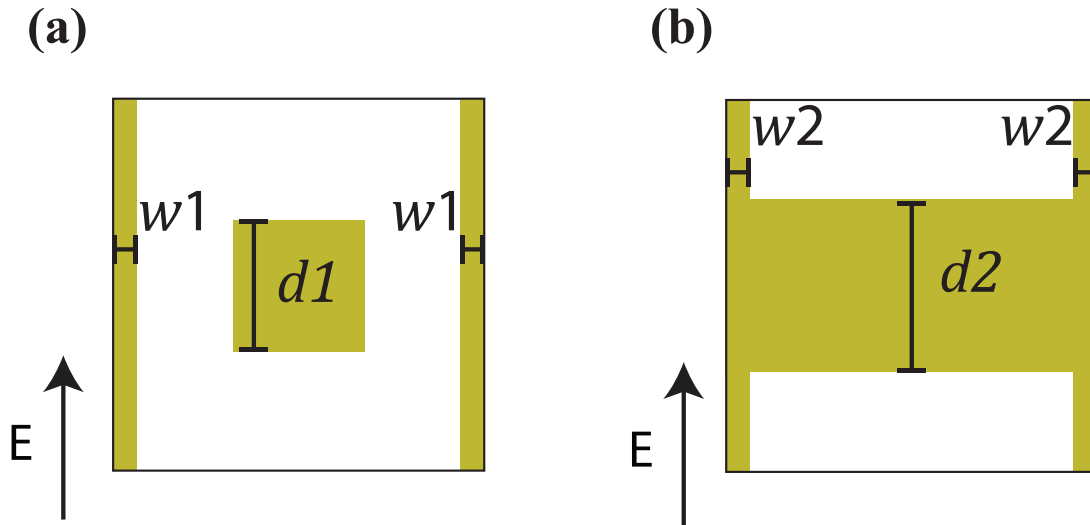


**Figure S5: (a)** Proposed geometry that has an identical operation as the geometry presented in the main text (see Figure 2(c)) for the polarization shown. **(b)** Fishnet geometry. The fishnet geometry has a larger capacitance and correspondingly smaller inductance than the proposed geometry.

Let both geometries have a resonant frequency of $\omega_o = 1/\sqrt{L_1 C_1} = 1/\sqrt{L_2 C_2}$, where $L_1 > L_2$ and $C_1 < C_2$. The impedance of this structure is given by its parallel combination, $Z = \left(\frac{1}{j\omega L} + j\omega C + \frac{1}{R}\right)^{-1}$. The resistance ($R$) models the metallic loss and is assumed to be equal for both geometries. The impedance bandwidth is inversely proportional to its frequency derivative at resonance,

$$\frac{dZ}{d\omega} = \frac{jLR^2(1 + \omega^2 LC)}{R - \omega^2 RLC + j\omega L} \tag{s8}$$

Operating near resonance, $\omega = \omega_o$, $C = 1/(\omega_o^2 L)$, it can be seen that the frequency derivative is inversely proportional to the inductance,

$$\left(\frac{dZ}{d\omega}\Big|_{\omega=\omega_o}\right) = \frac{-j2R^2}{L\omega_o^2} \tag{s9}$$

Thus, to achieve a maximal bandwidth, the inductance should be maximized and the capacitance should be minimized. However, it should be noted that this analysis is only accurate when the spacing between metallic sheets along the $z$ axis is large enough that evanescent coupling can be neglected. When realizing bulk negative index metamaterials, the spacing between metallic sheets is usually reduced from the 200 nm spacing used here, and there is significant evanescent coupling between the sheets.[6-7]

**Designed and fabricated dimensions**

The beam-refracting Huygens' surface presented in the main text consists of five unique unit cells. Using the naming convention of Figures 2(a), 2(c), and 3(a) of the main text, the designed dimensions of each unit cell are provided in Table S1. The subscripts 1, 2, and 3 denote the dimensions of the first, second, and third layers, respectively.

| Cell# | $Y_{s1}$ | | $Y_{s2}$ | | $Y_{s3}$ | |
| --- | --- | --- | --- | --- | --- | --- |
| | $w_1$ | $d_1$ | $w_2$ | $d_2$ | $w_3$ | $d_3$ |
| 1 | 166 | 0 | 212 | 0 | 206 | 0 |
| 2 | 78 | 0 | 110 | 0 | 110 | 0 |
| 3 | 60 | 278 | 60 | 210 | 60 | 214 |
| 4 | 60 | 324 | 60 | 298 | 60 | 270 |
| 5 | 60 | 364 | 60 | 306 | 60 | 296 |

**Table S1:** Designed dimensions (nm) of each sheet admittance that provide the simulated performance presented in Figures 3 and 4 of the main text.

However, the dimensions that were fabricated using the process detailed in Figure 5(a) of the main text were off by ~30 nm from the designed dimensions. As measured from SEM pictures,

the fabricated dimensions of each layer are shown below. The updated simulation results shown in Figure 6 of the main text assume the dimensions of all three sheets are equal to the middle layer.

| Cell# | $Y_{s1}$ | | $Y_{s2}$ | | $Y_{s3}$ | |
|---|---|---|---|---|---|---|
| | $w_1$ | $d_1$ | $w_2$ | $d_2$ | $w_3$ | $d_3$ |
| 1 | 255 | 0 | 255 | 0 | 270 | 0 |
| 2 | 140 | 0 | 140 | 0 | 190 | 0 |
| 3 | 93 | 200 | 93 | 200 | 110 | 220 |
| 4 | 93 | 290 | 93 | 290 | 110 | 325 |
| 5 | 93 | 340 | 93 | 340 | 110 | 355 |

**Table S2:** Fabricated dimensions (nm) of each sheet admittance measured with SEM pictures. It can be seen that the fabricated dimensions are ~30 nm different from the design dimensions, which reduced the measured performance.

1.    Pozar, D. M., *Microwave engineering*. Wiley. com: 2009.
2.    Memarzadeh, B.; Mosallaei, H., Array of planar plasmonic scatterers functioning as light concentrator. *Optics Lett.* **2011,** *36* (13), 2569-2571, DOI: 10.1364/OL.36.002569.
3.    Monticone, F.; Estakhri, N. M.; Alù, A., Full control of nanoscale optical transmission with a composite metascreen. *Phys. Rev. Lett.* **2013,** *110* (20), 203903, DOI: 10.1103/PhysRevLett.110.203903.
4.    Pfeiffer, C.; Grbic, A., Cascaded metasurfaces for complete phase and polarization control. *Appl. Phys. Lett.* **2013,** *102*, 231116, DOI: 10.1063/1.4810873.
5.    Pfeiffer, C.; Grbic, A., Millimeter-Wave Transmitarrays for Wavefront and Polarization Control. *IEEE Trans. on Microwave Theory and Tech.* **2013,** *61* (12), 4407-4417, DOI: 10.1109/TMTT.2013.2287173.
6.    Zhang, S.; Fan, W.; Malloy, K.; Brueck, S.; Panoiu, N.; Osgood, R., Near-infrared double negative metamaterials. *Opt. Express* **2005,** *13* (13), 4922-4930, DOI: 10.1364/OPEX.13.004922.
7.    Valentine, J.; Zhang, S.; Zentgraf, T.; Ulin-Avila, E.; Genov, D. A.; Bartal, G.; Zhang, X., Three-dimensional optical metamaterial with a negative refractive index. *Nature* **2008,** *455* (7211), 376-379, DOI: 10.1038/nature07247.